

Supporting Information for

Two-Dimensional Pyramid-Like WS₂ Layered Structures for Highly Efficient Edge Second-Harmonic Generation

Xianqing Lin, Yingying Liu, Kang Wang, Cong Wei, Wei Zhang, Yongli Yan, Yong Jun Li, Jiannian Yao, and Yong Sheng Zhao*

Key Laboratory of Photochemistry, Institute of Chemistry, Chinese Academy of Sciences, Beijing 100190, China

University of Chinese Academy of Sciences, Beijing 100049, China

E-mail: yszhao@iccas.ac.cn

Table of Contents

1. **Figure S1.** Schematic of atmospheric pressure chemical vapor deposition method for WS₂ nanostructure growth.
2. **Figure S2.** Bright-field optical microscopy and AFM images of monolayer WS₂.
3. **Figure S3.** AFM images of the intermediates and illustration for the growth process of the P-multilayer WS₂.
4. **Figure S4.** Raman spectra for P-multilayer WS₂, exfoliated 2H-WS₂ and bulk WS₂.
5. **Figure S5.** Atomic resolution STEM–HAADF images of P-multilayer WS₂.
6. **Figure S6.** Height profile marked with a red line shown in the inset of Figure 1d.
7. **Figure S7.** Schematic demonstration of the experimental setups for optical characterization.
8. **Figure S8.** Simulated electric field distribution in monolayer WS₂ on SiO₂/Si and silver substrates.

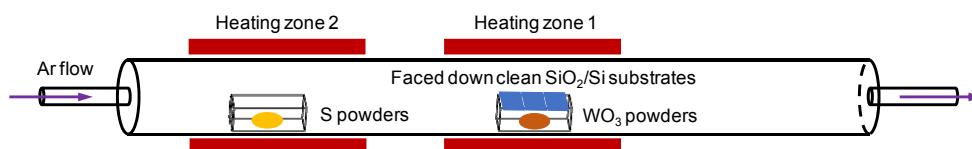


Figure S1. Schematic of atmospheric pressure chemical vapor deposition method for WS_2 nanostructures growth.

As demonstrated in Figure S1, the synthesis of the 2D WS_2 nanostructures were carried out in a CVD system with two separated heating zones, so that the evaporation temperature of WO_3 and S powders can be separately controlled.¹ Before heating, the tube was vacuum pumped to evacuate the air and then refilled with high-purity argon (Ar) to atmospheric pressure. During the growth process, high-purity Ar is continuously supplied as the carrier gas.

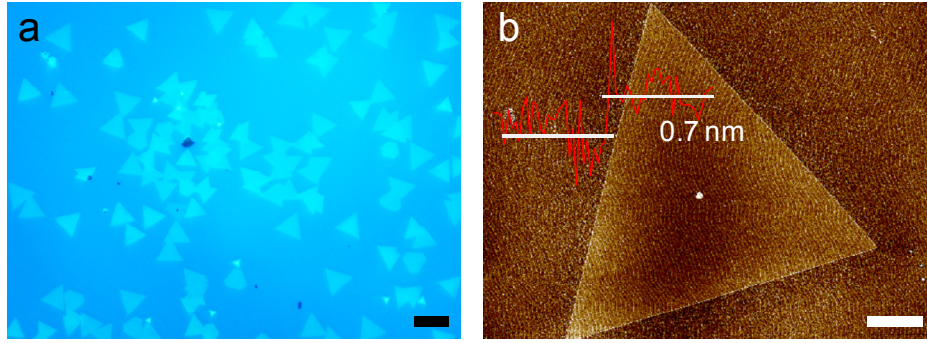


Figure S2. (a) Bright-field optical microscopy image of monolayer WS₂ prepared by CVD method. Scale bar is 15 μm. (b) AFM image of a typical monolayer WS₂. Scale bar is 2 μm.

As demonstrated in Figure S2, monolayer WS₂ nanostructures were obtained when the flow rate of carrier gas is 400 sccm. The monolayer WS₂ belongs to D_{3h} space group with broken inversion symmetry, resulting in non-vanishing second order nonlinear susceptibility,²⁻⁴ which is beneficial to obtain efficient SH radiation.

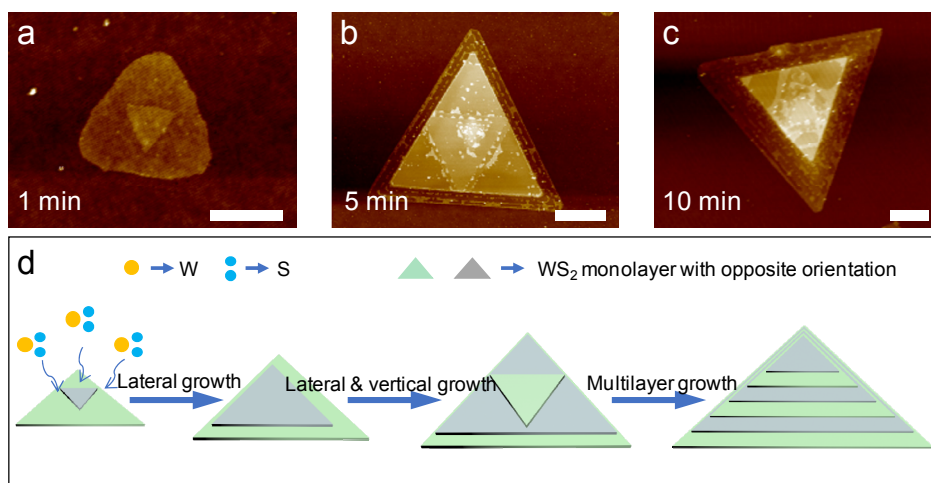


Figure S3. (a-c) AFM images of the observed intermediates obtained at different growth stages. (a) 1 min; (b) 5 min; (c) 10 min. All scale bars are 1 μm . (d) Illustration for the growth process of the P-multilayer WS₂.

Figure S3a-c show the AFM images of the representative single WS₂ flakes with the growth times of 1, 5, and 10 min, respectively. For the growth time of 1 min at 930 °C, AB-stacked bilayer WS₂ nanosheets with rough edges were obtained (Figure S3a). With the increasing of growth time (5 min), both the in-plane and out-plane of WS₂ grows dramatically, as demonstrate in Figure S3b. Then, a typical P-multilayer WS₂ nanosheets (Figure S3c) were obtained with further expending the growth time. The growth process of P-multilayer WS₂ is schematically demonstrated in Figure S3d. At the initial stage, the thermodynamically stable bilayer WS₂ with preferred 2H stacking grown at the surface of SiO₂/Si substrate during the vaporization of the source materials. Then, as the existence of dangling bonds at the rough edges, the obtained WS₂ flake would continue to grow in the lateral directions. Moreover, because the multilayer WS₂ structure is thermodynamically favorable, both the lateral and vertical directions would grow with the increasing of the growth time. The sequentially decreased growth time from the bottom to the top layers naturally, along with the decreasing supply of source materials, leads to the gradually decreasing of basal planes of multilayer WS₂ flakes. Consequently, P-multilayer WS₂ structures were obtained. These as-fabricated P-multilayer WS₂ structures facilitate the investigation of edge SHG.

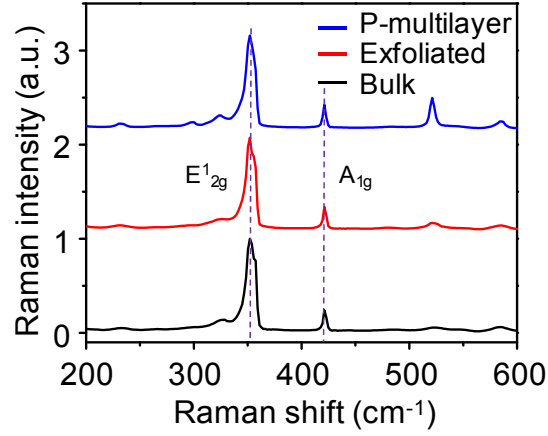


Figure S4. Raman spectra for P-multilayer WS₂ (blue), exfoliated 2H-WS₂ (red) and bulk WS₂ (black).

As we can see from Figure S4, the Raman shift of P-multilayer WS₂ is consistent with those of exfoliated 2H-WS₂ and bulk WS₂. This indicates that the as-prepared P-multilayer WS₂ has the same structure with bulk WS₂, further confirming the AB stacking growth mode of P-multilayer WS₂.

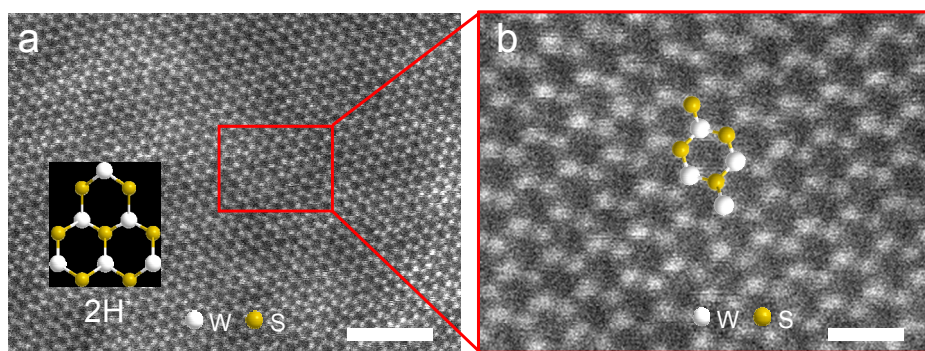


Figure S5. (a) Atomic resolution STEM–HAADF images of P-multilayer WS₂. Scale bar is 2 nm. Inset: schematic structure of the unit cells of 2H stacking order. (b) Magnified view of the region marked with red box in (a). Scale bar is 0.5 nm.

The atomic resolution STEM–HAADF images show the uniform hexagonal arrangement of W and S atoms, which agrees well with that of TMDs with 2H stacking order.⁵⁻⁷ This indicates that the as-prepared P-multilayer WS₂ has good alignment of all the layers and well-defined AB stacked configuration.

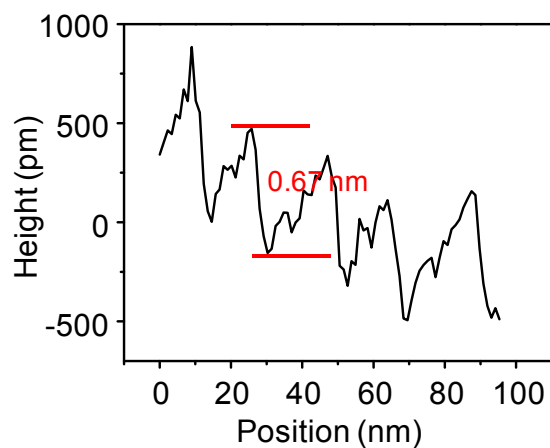


Figure S6. Height profile marked with a red line shown in the inset of Figure 1d.

As plotted in Figure S6, the step height of P-multilayer WS₂ is measured to be ≈ 0.67 nm, close to the thickness of a WS₂ monolayer,⁸ which confirms that the basal planes of P-multilayer WS₂ flake shrunk gradually from the bottom to the top layers. This structure facilitates the investigation of edge SHG.

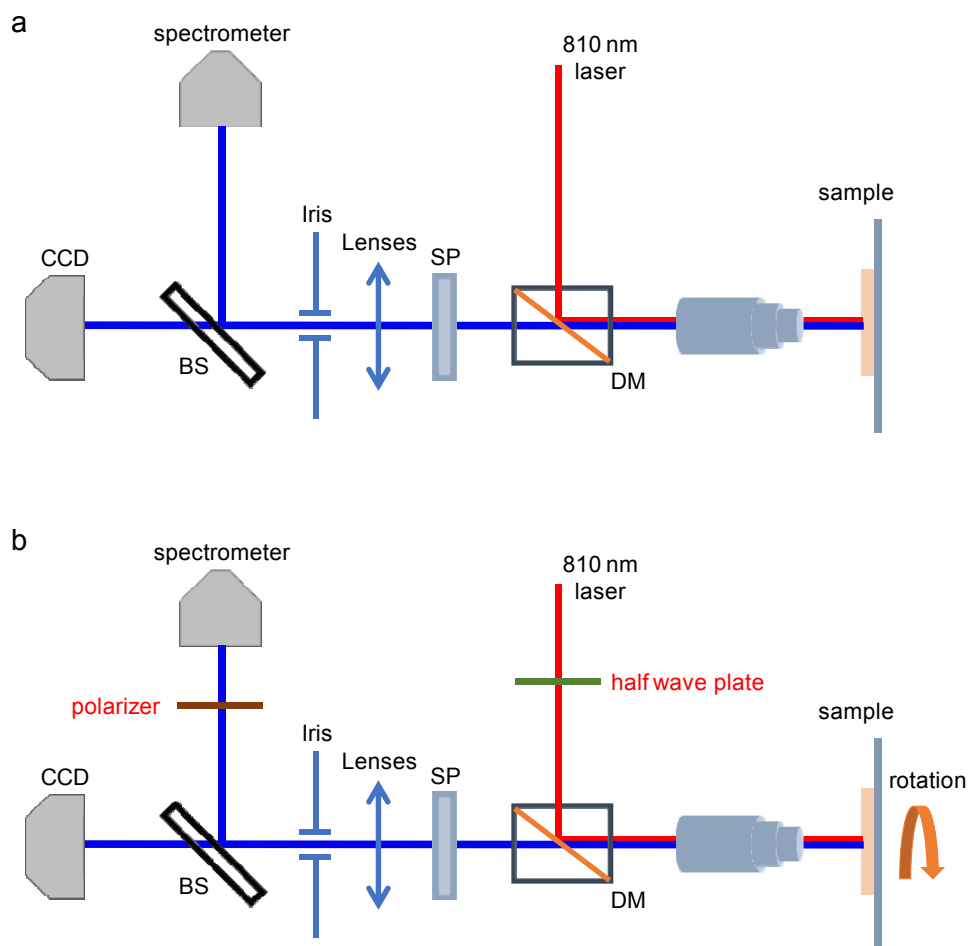


Figure S7. Schematic demonstration of the experimental setups for optical characterization.

As illustrated in Figure S7a, The SH measurements were performed in a reflection geometry using normal incidence excitation. The WS₂ nanostructures were excited locally with a Ti:sapphire laser (Chameleon Vision II) focused down to 4 μm diameter spot through an objective (Nikon CFLU Plan, 50x, N.A.=0.8) to obtain SH radiation. The excitation laser (FW) was filtered with a 750 nm short-pass filter. The emission from the WS₂ nanostructure was dispersed with a grating (150 G/mm) and recorded with a thermal-electrically cooled CCD (Princeton Instruments, ProEm: 1600B). For polarization dependent SHG measurements, as shown in Figure S7b, the polarization of FW signals was altered with a half wave plate. A polarizer with a fixed polarization was placed in front of spectrometer to select the parallel components of the SH radiation with respect to the polarization of FW (parallel polarization configuration). In this setup, the samples were freely rotated to obtain the orientational dependence of the SH response.

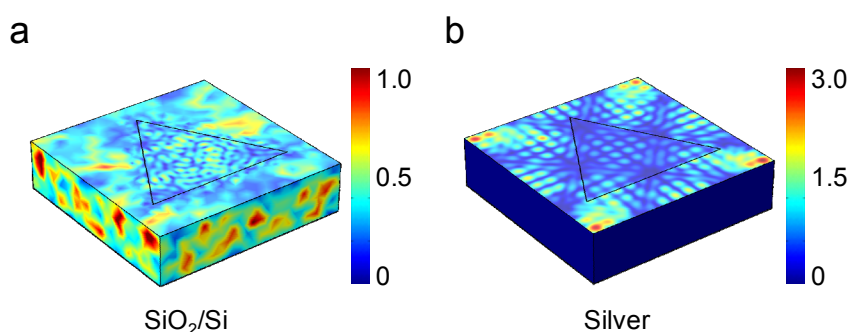


Figure S8. Simulated electric field distribution in monolayer WS₂ on SiO₂/Si and silver substrates.

As shown in Figure S8, due to the atomic thickness of monolayer WS₂, FW signals cannot be confined in monolayer WS₂ on SiO₂/Si or silver substrates. For the monolayer WS₂ on SiO₂/Si substrate, most of the electric field is distributed in the substrate (Figure S8a). By contrast, due to the high reflection efficient of silver film, the electric field is confined around the interface between WS₂ and silver substrate in hybrid plasmonic structure (Figure S8b).⁹ This results in tiny enhancement of SHG in monolayer WS₂ hybrid plasmonic structure with respect to that from monolayer WS₂ on SiO₂/Si substrate.

References:

1. Rong, Y.; Fan, Y.; Leen Koh, A.; Robertson, A. W.; He, K.; Wang, S.; Tan, H.; Sinclair, R.; Warner, J. H. Controlling Sulphur Precursor Addition for Large Single Crystal Domains of WS₂. *Nanoscale* **2014**, *6*, 12096-12103.
2. Kumar, N.; Najmaei, S.; Cui, Q. N.; Ceballos, F.; Ajayan, P. M.; Lou, J.; Zhao, H. Second Harmonic Microscopy of Monolayer MoS₂. *Phys. Rev. B* **2013**, *87*, 161403.
3. Malard, L. M.; Alencar, T. V.; Barboza, A. P. M.; Mak, K. F.; de Paula, A. M. Observation of Intense Second Harmonic Generation from MoS₂ Atomic Crystals. *Phys. Rev. B* **2013**, *87*, 201401.
4. Clark, D. J.; Senthilkumar, V.; Le, C. T.; Weerawarne, D. L.; Shim, B.; Jang, J. I.; Shim, J. H.; Cho, J.; Sim, Y.; Seong, M. J.; Rhim, S. H.; Freeman, A. J.; Chung, K. H.; Kim, Y. S. Strong Optical Nonlinearity of CVD-grown MoS₂ Monolayer as Probed by Wavelength-Dependent Second-Harmonic Generation. *Phys. Rev. B* **2014**, *90*, 121409.
5. Yan, J.; Xia, J.; Wang, X.; Liu, L.; Kuo, J. L.; Tay, B. K.; Chen, S.; Zhou, W.; Liu, Z.; Shen, Z. X., Stacking-Dependent Interlayer Coupling in Trilayer MoS₂ with Broken Inversion Symmetry.

Nano Lett. **2015**, *15*, 8155-8161.

6. Puretzky, A. A.; Liang, L.; Li, X.; Xiao, K.; Wang, K.; Mahjour-Samani, M.; Basile, L.; Idrobo, J. C.; Sumpter, B. G.; Meunier, V.; Geohegan, D. B., Low-Frequency Raman Fingerprints of Two-Dimensional Metal Dichalcogenide Layer Stacking Configurations. *ACS Nano* **2015**, *9*, 6333-6342.
7. Lu, X.; Utama, M. I.; Lin, J.; Gong, X.; Zhang, J.; Zhao, Y.; Pantelides, S. T.; Wang, J.; Dong, Z.; Liu, Z.; Zhou, W.; Xiong, Q., Large-Area Synthesis of Monolayer and Few-Layer MoSe₂ Films on SiO₂ Substrates. *Nano Lett.* **2014**, *14*, 2419-2425.
8. Cong, C.; Shang, J.; Wu, X.; Cao, B.; Peimyoo, N.; Qiu, C.; Sun, L.; Yu, T. Synthesis and Optical Properties of Large-Area Single-Crystalline 2D Semiconductor WS₂ Monolayer from Chemical Vapor Deposition. *Adv. Opt. Mater.* **2014**, *2*, 131-136.
9. Liu, X.; Zhang, Q.; Chong, W. K.; Yip, J. N.; Wen, X.; Li, Z.; Wei, F.; Yu, G.; Xiong, Q.; Sum, T. C. Cooperative Enhancement of Second-Harmonic Generation from a Single CdS Nanobelt-Hybrid Plasmonic Structure. *ACS Nano* **2015**, *9*, 5018-5026.